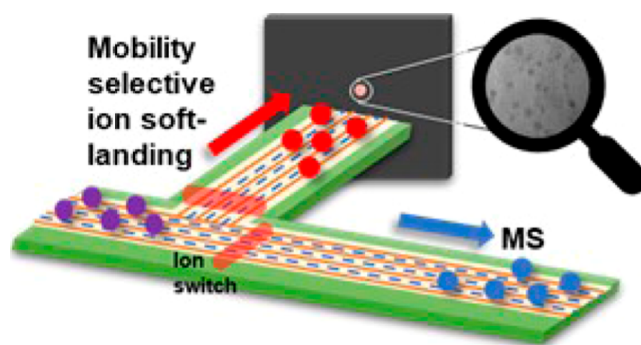


Mobility Selective Ion Soft-Landing and Characterization Enabled Using Structures for Lossless Ion Manipulation

Jung Y. Lee,[§] Ailin Li,[§] Venkateshkumar Prabhakaran, Xin Zhang, Christopher P. P. Harrilal, Libor Kovarik, Yehia M. Ibrahim, Richard D. Smith, and Sandilya V. B. Garimella*

ABSTRACT: While conventional ion-soft landing uses the mass-to-charge (m/z) ratio to achieve molecular selection for deposition, here we demonstrate the use of Structures for Lossless Ion Manipulation (SLIM) for mobility-based ion selection and deposition. The dynamic rerouting capabilities of SLIM were leveraged to enable the rerouting of a selected range of mobilities to a different SLIM path (rather than MS) that terminated at a deposition surface. A selected mobility range from a phosphazene ion mixture was rerouted and deposited with a current pulse (~ 150 pA) resembling its mobility peak. In addition, from a mixture of tetra-alkyl ammonium (TAA) ions containing chain lengths of C5–C8, selected chains (C6, C7) were collected on a surface, reconstituted into solution-phase, and subsequently analyzed with a SLIM-qToF to obtain an IMS/MS spectrum, confirming the identity of the selected species. Further, this method was used to characterize triply charged tungsten-polyoxometalate anions, $\text{PW}_{12}\text{O}_{40}^{3-}$ (WPOM). The arrival time distribution of the IMS/MS showed multiple peaks associated with the triply charged anion ($\text{PW}_{12}\text{O}_{40}^{3-}$), of which a selected ATD was deposited and imaged using TEM. Additionally, the identity of the deposited WPOM was ascertained using energy-dispersive (EDS) spectroscopy. Further, we present theory and computations that reveal ion landing energies, the ability to modulate the energies, and deposition spot sizes.



■ INTRODUCTION

Patterning surfaces with specific molecules is an area of interest for multiple applications. For example, patterned biomacromolecules (i.e., microarrays or “chips”) produce a sample format suited to automated analysis for biological activity;^{1,2} notably, the widely used “DNA chip”, where a high spot density ($\sim 10,000$ spots/ cm^2) is created by automated procedures depositing specific nucleotides at preselected positions. Techniques developed for the deposition of macromolecules onto solid supports like microdispensing,³ electrospray deposition,⁴ robotic printing,⁵ and ink jet deposition⁶ are useful but require appropriate sample extraction and purification steps and the fine-tuning of conditions for accurate and specific binding to the surface. The use of mass spectrometry (MS) for achieving such purification and isolation steps with high specificity has been an ongoing area of interest. While preparative separations using MS have been known for some time,⁷ the low material deposition rates have limited the applicability of the method. Meanwhile, ongoing work has enabled significant improvement in the throughput of deposition using high-flux instrumentation.^{8–10} Also, increasing selectivity of the method for isolation

and collection for material isolation at high purity has been aspirational and of ongoing interest.

Ion soft landing (ISL) is a preparative MS-based deposition process in which selected gas-phase ions of interest are concentrated into a beam and deposited in vacuum as thin film coatings at energies low enough to preserve the structural and functional integrity of the deposited molecules.⁹ The ISL deposition technique presents significant potential for practical uses,^{11–13} ranging from material synthesis for batteries and nanoelectronics to selective deposition of bioparticles from complex protein assemblies. In ISL, sorting/separation of ions is typically performed based on the mass-to-charge ratio (m/z). The typical ISL instrumentation consists of an ionization source, ion optics for guiding ion trajectories, a m/z filter (or some m/z -based isolation platform) for separation and selection of ions of interest, and a surface onto which ions

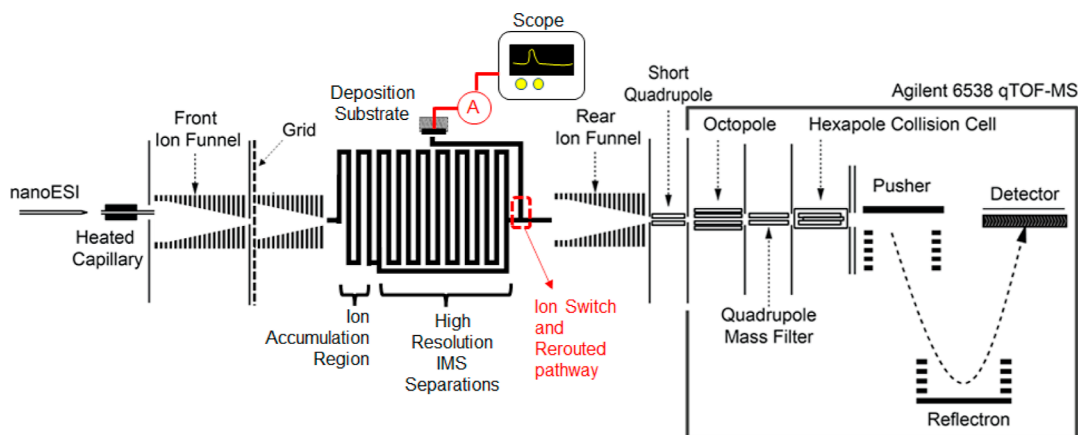


Figure 1. Schematic of the SLIM-MS instrumentation used for high-resolution IMS separations and selective deposition.

are deposited. As with MS systems, m/z selection typically occurs in a relatively high vacuum (e.g., $<10^{-2}$ Torr). Extensive works for optimal collection and subsequent characterization of ionic species from low kinetic energies (soft landing) or reactive landing and with controlled kinetic energies have been reported.^{8,9,14,15} ISL has been used to gain structural information on biological molecules (i.e., large proteins and viruses) due to its ability to largely preserve biological activity and conformations.^{16,17} For example, in biomedical applications such as the synthesis and coating of particles and proteins used for disease diagnosis¹⁸ and drug delivery vehicles,^{19,20} high selectivity enabled by mass selection alone or in combination with structural separations prior to deposition plays a key role in developing an understanding at the molecular level. In combination with rapidly advancing ultrahigh-resolution imaging technologies (i.e., cryo-EM,¹³ low-energy electron holography,²¹ scanning probe microscopy,²² and scanning tunneling microscopy²³) ISL has recently been shown as an emergent approach to enable the characterization of molecular structures at the single-molecule level. For example, ISL was used to create a high-purity sample by mass-selecting for cryo-EM imaging of biomolecules¹³ as it allows for separation from aggregates, fragments, and molecules with altered structures, which are commonly produced in the conventional cryo-EM sample preparation process. Images of soft-landed molecules showed no conformational variability among deposited molecules, making it possible to distinguish different structural features.

While the utility of the ISL to probe molecules has been significant, extensive instrumentation is necessary for mass selection. When selective deposition is performed under ambient/atmospheric pressure conditions, instrumentation, collection, and sample retrieval^{24,25} are simplified, albeit lacking in selectivity. Under ambient conditions, for example, polyoxometalates (POM) ions were deposited to prepare redox supercapacitor devices²⁶ and integrated photoelectrochemical energy storage cells²⁷ which displayed comparable energy storage performance to those with POM deposited in vacuum, in addition to showing promise in terms of high ionic current leading to an increased deposition rate.^{28,29} The ability to scale ion current and ease of instrumentation for soft-landing under atmospheric pressure conditions, however, comes at the detriment of the selectivity of ionic species. Also, an added challenge under atmospheric pressure conditions is the relatively poorer control over the ion

beam's spatial distribution due to inefficient ion confinement and collisions with neutrals.

Improved selectivity (e.g., MS separation resolving power) in combination with the ability to handle relatively large molecular sample quantities (i.e., with minimal ion loss) is the key to enabling precise control over the deposition process with minimal introduction of impurities and suitability in various applications such as nanofabrication, surface functionalization, and molecular characterization. Particularly, high-resolution separations have become increasingly desirable for the selective deposition of specific molecular compounds within heterogeneous ensembles. Many ion mobility separation platforms have been explored previously that attempt to simultaneously soft-land molecules, notably one that used soft-landing ion mobility (also abbreviated as "SLIM" in literature) for sub-eV deposition of ions and nanocluster deposition.^{30–32} In other work, a differential mobility analyzer with periodic focusing (achieved using a combination of lateral electric fields and gas flows) for portable analysis has parallel utility in collecting selective ion mobilities onto surfaces.³³

In recent years, the coupling of MS to the structurally sensitive ion separation platform, Structures for Lossless Ion Manipulations (referred to as SLIM), developed by our group has been successfully applied to distinguish molecular classes³⁴ and structurally similar molecules with ultrahigh resolution mobility-based separations^{35,36} toward applications in multiomics analyses, environmental monitoring, and numerous other areas. Here, we demonstrate a method for utilizing SLIM for high-resolution ion mobility separations, followed by the isolation of a selected range of mobilities for ISL with subsequent characterization/confirmation of the deposited species using MS, TEM, and other spectroscopic techniques. The initial demonstration of the use of SLIM for soft-landing platforms opens new opportunities for isomer selective ion deposition with high selectivity, as well as combined m/z and mobility selective deposition, with broad utility for molecular structure determination when used in conjunction with orthogonal characterization techniques like cryoEM, spectroscopy, etc.

■ EXPERIMENTAL SECTION

SLIM and Mass Spectrometry Instrumentation. The schematic of the instrumentation used for this work is shown in Figure 1. Ions were introduced into the system using a nanoelectrospray ionization source. A syringe pump (Fusion

100, Chemyx Inc., Stafford, TX, USA) was used to infuse the sample solution into the ionization source at flow rates between 1 and 5 $\mu\text{L}/\text{min}$, and an ionization voltage of 4000 V. Upon ionization, the ions were sampled into a heated transfer capillary (maintained at 140 °C and a DC voltage of 380 V) and delivered to the vacuum stages of the SLIM-qTOF instrument. Ions from the heated capillary entered a region of ~ 10 Torr pressure where a front ion funnel sampled the incoming ion plume and delivered it toward the next downstream pressure stage. The front funnel had radio frequency voltages of 300 $V_{\text{p-p}}$ for confinement and a DC gradient of 10 V/cm. The voltage drop across the front ion funnel was 100 V, from 340 to 240 V. The front ion funnel culminated in an electrode plate carrying a voltage of 245 V that served additionally as a flow conductance limit to the next pressure stage.

Downstream of the front ion funnel, a second pressure chamber maintained at 3 Torr pressure of N_2 gas houses a low-pressure ion funnel and the SLIM setup. The low-pressure ion funnel had a radiofrequency voltage of 300 $V_{\text{p-p}}$ and, a dc voltage drop of 240 to 160 V. Just upstream of the low-pressure ion funnel a dc grid was mounted that was biased with a dynamic dc voltage to enable timed block and release of ions into the SLIM. A voltage of 245 V on the grid allowed ions to travel toward the SLIM, and a blocking voltage of 345 V killed the ion beam, preventing transmission to the SLIM. The SLIM system itself was biased at 150 V to enable the entry of ions incoming from upstream ion optics into the SLIM system. The voltage values for each element are detailed in the Supporting Information (Table S1).

The SLIM configuration has been described in detail previously.³⁷ Briefly, the SLIM design utilized electrode arrangements patterned on printed circuit boards having ion paths using 6 rf electrodes (i.e., electrodes that carry radio frequency (rf) voltages for ion confinement) interspersed with segmented traveling wave (TW) electrodes each 1 mm in length. A TW profile of 50% duty cycle square wave (i.e., 4 TW electrodes at a high voltage and subsequent 4 TW electrodes at a low voltage) was employed to create the separation voltages on the SLIM. In addition to confinement and separation, the SLIM platform enabled complex ion manipulations (*viz*, serpentine path³⁸ and multipass separations³⁶). In the present work, a single-pass separation was performed with a separation path length of ~ 8 m and a separation time of less than a second.

The SLIM boards were biased at 150 V, and all the voltage parameters for different SLIM electrodes are relative to this bias. SLIM DC guard voltage (5 V) and RF potentials (300 $V_{\text{p-p}}$) with 1 MHz frequency were used for ion confinement. The TW speed used for ion separations was 128 m/s (electrode-to-electrode voltage stepping frequency of 16 kHz), and the TW amplitude was 30 $V_{\text{0-p}}$. The pressure inside the SLIM chamber was held at 3 Torr. The SLIM board possessed an ion switch³⁹ to reroute ions to a path that culminated at a deposition substrate. The ion switch was operated as reported previously⁴⁰ and enabled rerouting a temporally selected ion mobility window of arbitrary width to the deposition region. This width could be as small as 500 μs and as large as the length of the experiment, and an arbitrary number of such windows could be programmatically used during an acquisition if desired. The conductive deposition substrate in Figure 1 was grounded through a current amplifier (Stanford Research Systems, model SR570) to measure the

deposition ion beam current and further connected to an oscilloscope (Tektronix model TDS5104B) for data recording and retrieval. The current measurement was set up in a manner that enabled capture of the pulsed ion current (corresponding to a selected ion mobility peak) that periodically arrived at the substrate. The current measurement was triggered with the beginning of an ion mobility experiment, or, in other words, when an ion packet was injected for an IMS separation, and the current measurement recorded the peaks corresponding to those that were routed to the deposition substrate. Since the current amplifier and the substrate were grounded, effective voltage drops of 150 V were enforced between the SLIM and substrate for the ions routed for deposition. In lieu of the deposition substrate, different conductive surfaces were used to enable subsequent characterization (e.g., TEM grids, Cu grids, etc.). Ions not directed toward the deposition substrate exited the SLIM into a rear ion funnel, followed by q-TOF MS interfaced using a short-quadrupole.

Materials. An ESI low-concentration tuning mixture was obtained from Agilent Technologies (Santa Clara, CA). A mixture of tetra-alkyl ammonium (TAA) ions containing tetrapentylammonium (C5), tetrahexylammonium (C6), tetraheptylammonium (C7), and tetraoctylammonium (C8) ions was dissolved in acetonitrile to a final concentration of 1 μM . To enable retention of the deposited TAA ions on the substrate, a thin film of 1 μL of glycerol was created on the carbon substrate by pipetting and dispersing it. Phosphotungstic acid hydrate ($\text{H}_3[\text{PW}_{12}\text{O}_{40}]\cdot\text{XH}_2\text{O}$) was purchased from Sigma-Aldrich (St. Louis, MO). The WPOM solution for the ion soft-landing experiments was prepared by creating a 1 μM solution in methanol.

Transmission Electron Microscopy. Morphological characterization of the deposited WPOM was performed using an FEI Titan transmission electron microscope (Hillsboro, OR). Tungsten-polyoxometalate (WPOM) anions in the selected arrival time window were deposited onto TEM grids for 10 h. The samples were imaged using an accelerating voltage of 300 kV.

Energy Dispersive Spectroscopy (EDS). The chemical composition and distribution of the samples were analyzed by energy-dispersive X-ray spectroscopy (EDS) mapping with an Oxford X-Max 80 EDS detector (Oxford Instruments Analytical Ltd.) combined with an aberration-corrected electron microscope (FEI, Model Titan 80–300) in the STEM mode. STEM images were obtained at 300 keV by using a high-angle annular dark field (HAADF) detector. Data analysis was performed using a Gatan's Digital Micrograph 1.9.4. The STEM sample preparation was the same as for TEM.

Simulations. SIMION 8.2 (Adaptas Solutions LLC, Palmer, MA, USA) was used for performing ion trajectory simulations and kinetic energy calculations as the ions approached and landed on the deposition substrate. The SLIM module was built commensurate with the SLIM board designs, along with the deposition substrate, as the setup in the experiment. The statistical diffusion simulation (SDS) model^{41–43} available within SIMION was used to simulate collisions between the ions and neutrals with consideration of collisional damping effects and the thermalized motion of ions. The electrical field and pressure conditions used were identical to the physical conditions used in the experiment, as described above. Nitrogen gas was used with a mass of 28 amu and a molecular diameter of 0.3 nm. A pressure of 3 Torr was used

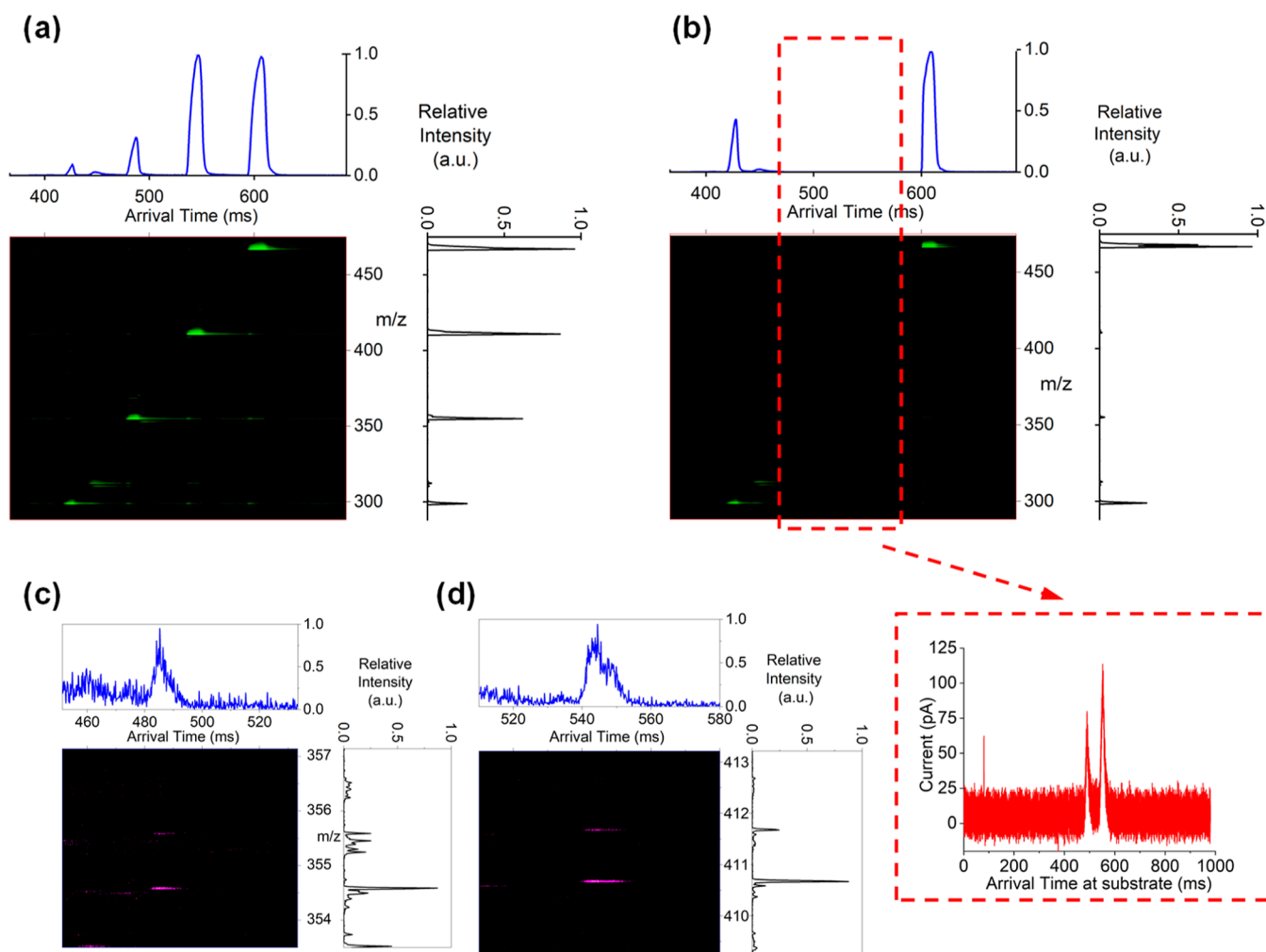


Figure 2. Arrival time distributions (top) and mass spectra (right) corresponding to (a) tetraalkylammonium (TAA) mixture containing chain lengths of C5–C8. (b) TAA mixture with C6 and C7 selectively routed to the deposition substrate and hence missing in the portion of spectrum rerouted to MS inset in the dotted red box shows the current measurement by the scope corresponding to a single acquisition of arrival times of C6 and C7 recorded at the deposition substrate. (c) C6 and (d) C7. The ions in the TAA mixture were mobility-selected for soft landing, and the deposition was dissolved in solution and infused for IMS-MS.

for all simulations. Diffusion and collision damping parameters were both enabled in the SDS model. The background gas temperature was set at 300 K. The time step of the simulation was enforced to be kept below 0.1 μ s. This was chosen to capture the effects of time-varying voltages, like radiofrequency voltages applied to the SLIM rf electrodes. Since rf voltages of frequency 1 MHz were used in the simulation and experiment, the time step used was 0.1 μ s or lower. Traveling wave (TW) with frequency 16 kHz and amplitude 30 V_{0-p} were used, and the TW profile was square waves with 50% duty cycle. The simulated ion population (masses and charges detailed in Supporting Information Table S2) included various compounds (of different mass and charge ranges and including WPOM ions). Each compound was represented by 200 charged particles in the simulation.

RESULTS AND DISCUSSION

Initially, a mixture containing different phosphazene ions (from the Agilent tuning mix) was used to demonstrate ion deposition via mobility or arrival-time based selection. A peak of m/z 922 (from among the other phosphazene species) was selectively rerouted by selecting its arrival time distributions

(ATD) to switch towards the deposition substrate while simultaneously measuring the current at the substrate. The measured current demonstrated the ability to deposit ions at a rate of ~ 73.5 billion ions per hour (as detailed in the Figure S1).

A similar experiment was performed using tetraalkyl ammonium ions (TAA). TAA consists of long alkyl chains attached to a central N^+ group, providing a particularly stable ion structure. A 1 μ M solution of TAA ions from ESI (Figure 2a) yielded four distinct mass peaks corresponding to C5, C6, C7, and C8 ions at m/z 298, 354, 410, and 466, respectively. (The 2D chemical structures of molecules are shown in Figure S2.) The two middle peaks (i.e., only C6 and C7 selected based on their ATDs) were then rerouted to the deposition substrate. The current measurements associated with this deposition are shown in Figure 2b inset, confirming that the peaks for C6 and C7 are arriving at the deposition substrate. To further confirm the identity of the deposited species, the selectively rerouted ions (corresponding to C6 and C7, i.e., $m/z = 354$ and 410) were, after 10 h of deposition onto a glassy carbon substrate, redissolved into the solution phase and infused into the SLIM-MS instrument. Considering the current

measured on the substrate (~ 80 and ~ 108 pA for the C6 and C7 peaks, respectively) and integrating under the current distribution peaks, 10 h deposition should yield 0.23 and 0.29 ng of material (corresponding to the peaks at m/z 354 and m/z 410, respectively) deposited on the substrate. For example, the peak associated with C7, upon integrating the current distribution over time, yielded a total charge of $Q = 1.863 \times 10^{-12}$ Coulombs. Since the charge state is $z = +1$, the total number of molecules associated with this charge would be $n = Q/1.602 \times 10^{-19}$ C, or $n = 1.162 \times 10^7$ molecules. Since this current was measured every acquisition, or every ~ 0.98 s, a 10 h deposition yielded $n_{\text{total}} = 10 \times 60 \times 60 \times 1.162 \times 10^7/0.98 = 42.719 \times 10^{10}$ molecules. For a m/z peak of 410 for C7, this constituted a mass of $m_{\text{deposition}} = 42.719 \times 10^{10} \times 409/N_A = 2900 \times 10^{-13}$ g = 0.29 ng. Due to the baseline noise of the current measurement, we can expect proportionate uncertainty in the measurement of the amount of material deposited with a $\sim 20\%$ standard deviation or an uncertainty of ± 0.05 ng.

Subsequently, the substrate was washed with 1 mL of methanol solution to form a solution of TAA (containing only the two peaks) and electro sprayed onto the instrument. To eliminate any carryover from previous experiments, a new sample delivery assembly consisting of an unused syringe, capillary, and ESI emitter was used to electro spray the deposited sample to obtain unambiguous confirmation of the deposited sample. Figure 2c,d report the electro spray ionization IMS/MS spectra for the selectively deposited species by rerouting a chosen portion of the arrival time distribution to the substrate. The full IMS/MS spectrum for the resprayed sample is shown in Supporting Information, Figure S3. The arrival times and differences in the arrival time between the two peaks match the expected values from the standard spectrum (Figure 2a). Also, the inset (in the box with a dotted red line) shows the current chromatogram (a single acquisition) recorded by the current amplifier at the deposition substrate and displays that the pulses of ion beam current to the substrate occur within the expected arrival time window, and the time interval between the two pulses corresponds to the arrival time difference. The Agilent tuning mix and TAA ions served to demonstrate the proof-of-concept for mobility or arrival time-selective ion deposition.

Figure 3a shows the IMS-MS spectrum of $\text{PW}_{12}\text{O}_{40}^{3-}$, a metal oxide with multielectron electrochemical properties. WPOM possesses multiple Keggin isomeric structures,⁴⁴ and we obtain arrival time distributions for the triply charged peak with multiple isomeric peaks with the SLIM IMS separation. Peak 1 displays a well-resolved distribution from other peaks (peaks 2 and 3, clearly visible, albeit not well separated). Peak 1 was rerouted for deposition and subsequent characterization. A TEM image of the deposited material is shown in Figure 3c (peak 1 shown, peak 2 deposition shown in Figure S6). These TEM experiments were performed by landing ions onto copper grids (Lacey Carbon, 300 mesh, copper grid, Ted Pella, Inc.). In Figure 3c, an empty portion of the substrate area (inside the green box) shows a diffraction pattern with nothing much to note. After noise removal and converting the diffraction pattern to an image (using FFT and iFFT in ImageJ⁴⁵) the area with no WPOM deposition is shown as the inset. For the area shown in the red box, a patch that visually appears as a carbon spot was investigated. The diffraction pattern again does not show any crystal structures, and the inverse with noise filters applied shows a dark spot with nothing much to note. Figure 3c (blue rectangles), however,

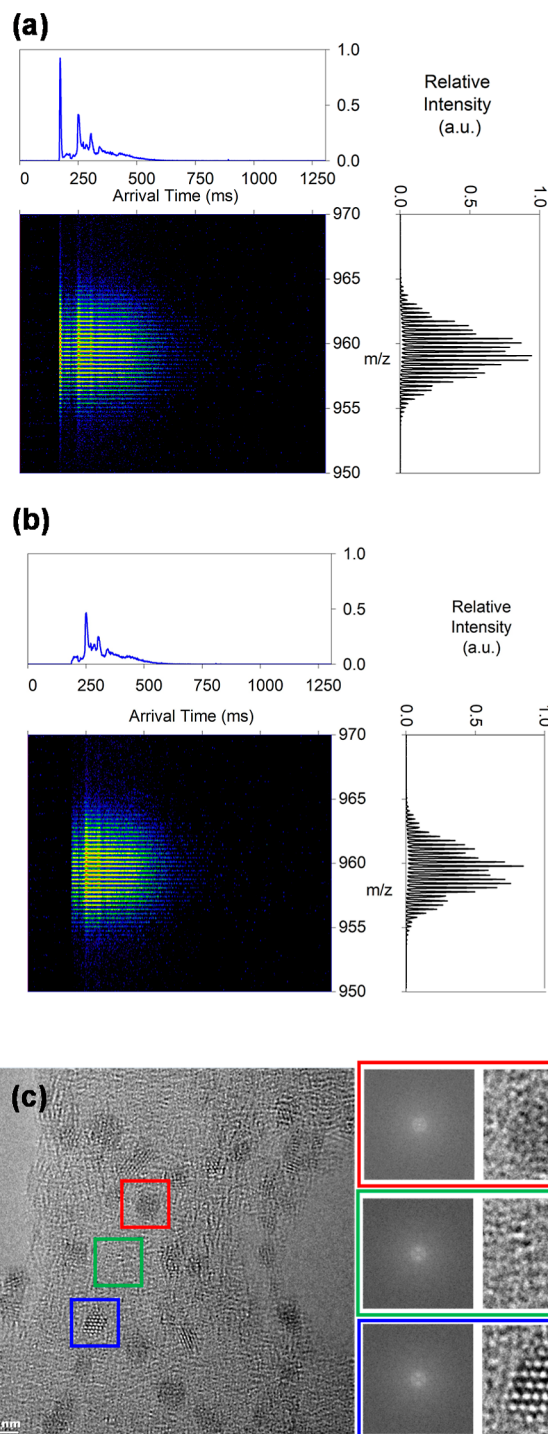


Figure 3. (a) ATD (top) and mass spectra (right) corresponding to $\text{PW}_{12}\text{O}_{40}^{3-}$. (b) Spectra with Peak 1 selectively routed to the deposition substrate and hence missing the portion of the spectrum rerouted to MS. (c) TEM image of Peak-1 deposited reveals clusters (in the blue box) compared to the substrate (green box) and hydrocarbon (red box).

shows deposited WPOM ions. In the absence of counterions during deposition, the formation of crystalline phases in the deposited POM anions may be attributed to the interaction of neutrals from the background environment.⁴⁶ This is likely due to the sample extraction and transport processes that take place in atmospheric conditions prior to TEM imaging. Minimizing the exposure to atmospheric conditions will likely provide

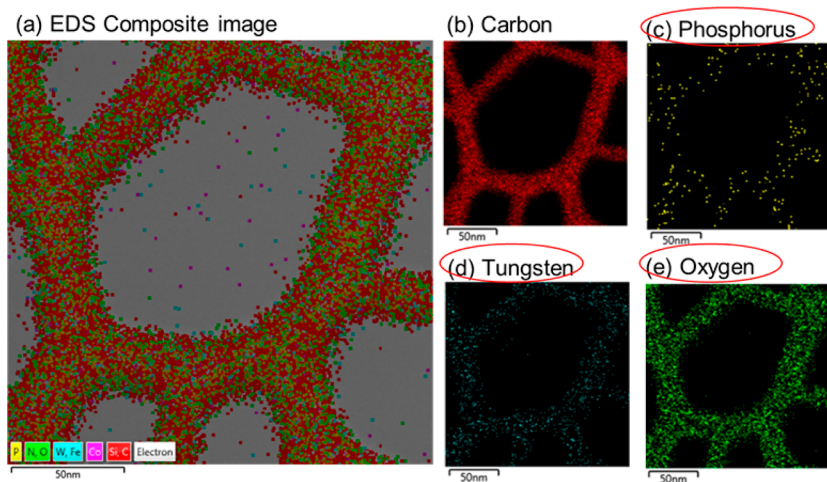


Figure 4. (a) EDS spectrum obtained from creating a composite image of all elemental signatures on the deposition, including (b) carbon, (c) phosphorus, (d) tungsten, and (e) oxygen.

better imaging resolution and characteristics, which will be investigated in future work. In addition, as will be discussed below, higher kinetic energies as ions land on the grounded substrate from the SLIM (biased at 150 V, i.e., across a 300 V/cm field) of ions during deposition could lead to POM ions being embedded into the substrate.

To confirm that the deposited and imaged structures correspond to WPOM, EDS spectra (Figure 4a–e) were obtained from the deposited sample. The EDS spectrum shows atomic signatures corresponding to the elements of WPOM. A copper grid was used to deposit WPOM, and the layered EDS image (Figure 4a) shows a composite image of all the elemental signatures (Figure 4b–e). Elements of tungsten and phosphorus are clearly deposited on the copper grids, indicating that the deposited material corresponds to WPOM.

Soft-landing of the ions is characterized by the low kinetic energy upon deposition and its impact on structural preservation. While other factors (e.g., a dehydrated environment under vacuum) may contribute some changes to the molecular structure of the deposited samples, we computed and analyzed the deposition energies to study the ion kinetic energies during the deposition process while using SLIM. As has been studied and established previously, SLIM separations tend to exhibit soft ion transport without significant ion activation due to being conducted in (typically a few Torr of) a buffer gas.⁴⁷ Thus, under generally soft ion transport/separation conditions, the kinetic energies at the deposition substrate are critical to establishing soft-landing, assuming that structures are generally preserved and gently transported inside SLIM. The SLIM system operated at ~ 3 Torr (see Methods section). At such pressures and under the prevailing electric fields, ions are generally thermalized (e.g., ions move at speeds that are scaled linearly by the electric field as a factor of the ion mobility), and significant activation (i.e., ion heating) is avoidable.

The kinetic energies upon landing were determined using simulations of the ion motion in the region, including the exit of SLIM and the deposition substrate. Figure 5a (left panel) shows the ion trajectory simulation, where ions traversing through the SLIM are then intercepted by the substrate. The electrostatic conditions used for simulations corresponded to the substrate being grounded and the SLIM at a voltage bias of 150 V (matching the condition where the experimental

measurements reported above were made). The simulated landing spot is indicated in Figure 5a (right panel), shown as the small bright spot in the black square background representing the deposition substrate. It is shown that ions are confined in a small spacing (~ 3 mm) between the SLIM surfaces, and the ion beam remains focused as it exits SLIM toward the substrate. Figure 5b shows the density plot of simulated ion distributions on the substrate (zoom-in view) with a bias of -150 V relative to the SLIM. The ions are distributed over an ellipse spanning roughly ~ 0.8 mm \times 0.5 mm as the ion beam travels fast enough to retain its elliptical shape that prevails during transport in SLIM. Figure 5c shows the spot size at -40 V bias of the substrate relative to the SLIM. The lower bias while landing (corresponding to lower speeds or kinetic energy of ions after exiting SLIM and as they arrive at the substrate) has a more circular and broader distribution of the ions (~ 1.5 mm diameter), as at lower speeds the ions tend to disperse with greater effects of ion diffusion between the SLIM and the substrate. The smaller spot size is a result of greater speed and, hence, higher kinetic energies of deposition. While intact deposition of large ions with kinetic energy up to 150 eV has been reported,^{48,49} softness of the landing process depends on a number of factors, including types of ions being deposited, landing surfaces, vacuum conditions, and kinetic energies.¹⁴ In other words, fragmentation and dissociative landing may occur at much lower collision energies as well, depending on the experimental specifics.⁵⁰ Our simulations predict that the biasing of the deposition substrate (not implemented in the experimental work reported here) can significantly reduce the kinetic energies of the ions, which may be mandatory for preserving the integrity of some molecules. The kinetic energies (ϵ_{ev}) can be easily modulated by biasing the landing substrate to an appropriate voltage due to the scaling law $\epsilon_{ev} \propto E_{dc}^2$ under low E/N conditions. The kinetic energies of the ions under constant field (drift tube conditions) are estimated theoretically (Figure S8a). More importantly, Figure 5d displays the simulated kinetic energies of different ion populations at the landing substrate (see Table S2 for the ions used) in the current SLIM system. Simulations were performed to match the prevailing operating conditions (SLIM bias = 150 V, TW amplitude = 30 V_{0,p}, substrate bias voltage = 0 V). The kinetic energies of landing are relatively low (4 eV and less) under the

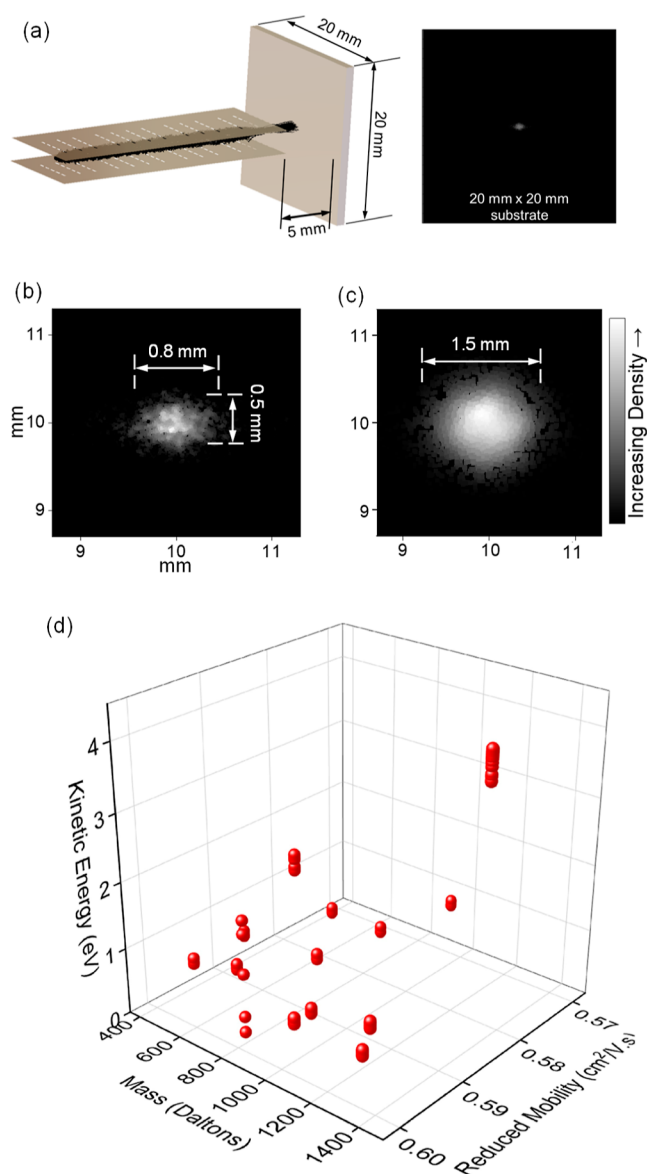


Figure 5. (a) Simulated ion trajectories through SLIM to the deposition substrate (left) and the spatial distribution of soft-landed ions on the substrate (right panel). Close-up view of deposited ions with the substrate bias of (b) -150 and (c) -40 V relative to SLIM. The color bar indicates the population density of the ions. (d) Kinetic energies of ions of various masses and mobilities at the landing substrate under experimental conditions where a -150 V bias exists between SLIM and the substrate.

operating conditions of many single-charged molecules. Specifically, the simulated average kinetic energy of triply charged WPOM anions is ~ 19 eV upon landing. Interestingly, these KE distributions were seen to be bimodal, which was more pronounced at lower KE of deposition (Figure S8b). Since the SLIM uses traveling waves (of amplitude $30 V_{0-p}$), the ions experience a temporally varying electric field as they proceed toward the landing substrate, resulting in a bimodal landing energy distribution. The electric fields can be easily modulated in the SLIM system without affecting the ability to separate and transport ions, but they vary the kinetic energies of deposition to achieve ISL. In our future work, we envision incorporating deposition interface designs (e.g., “mini-ion funnels”) and splash-landing⁵¹ on wet surfaces to both control

spot sizes and minimize any ion heating during deposition and study chemical systems where isomers are critical and have interesting structure-specific properties to be studied through orthogonal analysis.

CONCLUSIONS

Herein, we report our first demonstration of SLIM-enabled mobility selective deposition as a new approach for the preparation/production of molecular layers with improved selectivity and homogeneity. This method can leverage ultrahigh-resolution ion separations and selection with specificity toward molecular structures and conformations complementary to the conventional mass-selection-based ISL method. Mixtures of phosphazene ions and TAA salts with varying chain length are used to show the ability to selectively soft-land ions in a narrow mobility range without introducing other structurally similar species with comparable mobility. This is further supported by selectively depositing specific peaks associated with triply charged WPOM anions with electrochemical properties desirable for numerous applications. In TEM imaging with a nanometer resolution, deposited WPOM is easily distinguishable from the background, and its identity is confirmed using EDS. Our simulations show the ion kinetic energies upon impact range between 1 and 3 eV for a range of molecules with up to 2+ charges. Upon simulating the landing energies of $PW_{12}O_{40}^{3-}$, an energy of 19 eV was obtained. Compared to the literature published previously, these kinetic energy numbers for a range of molecules indicate comparable conditions to enable ISL. We envision future designs for the deposition region that will avoid any significant ion heating during deposition. In IMS-MS, the ion utilization efficiency is limited due to the requirement to completely block any ion flux into the ion separation region while mobility separation takes place. This leads to significant losses of incoming ions in the same time window. Given the soft-landing efficiency and deposition rate in our initial demonstration, different ion accumulation strategies developed by our group may be explored to further increase the throughput for deposition. For example, concurrent ion accumulation³⁷ and/or the array of ion traps⁵² are potential methods used to accomplish improvements in deposition rate. Complementary with conventional mass-selective deposition, SLIM-enabled mobility selection is advantageous with orthogonal ion separations, offering increased selectivity to produce a homogeneous sample with little conformational variability. The combination of this technique with advanced imaging technologies and a broad range of conventional spectroscopic techniques can be a potential method to enable improved molecular insight.

ASSOCIATED CONTENT

Supporting Information

Experimental current measurements of a selected arrival time distribution, followed by a discussion on how the current was measured and calculation of number of molecules, structures of TAA salts, raw data of tetra-alkyl ammonium (TAA) mixture with arrival time distributions without and with selective rerouting of peaks, raw data collected from electro spraying selected peaks deposited and reconstituted into solution and amplified

spectra of selected peaks for visual clarity, raw data of $\text{PW}_{12}\text{O}_{40}^{3-}$ ions with ATD showing three mobility peaks but with evidence of interconversion and peak tailing, TEM images of peak 2 of WPOM, simulated spatial distributions of deposited WPOM anions, theoretical and simulated kinetic energies of a variety of ion populations, followed by discussions on the effect of kinetic energy in the context of ISL, static voltages applied to all the components of the experimental setup, and list of ion populations used for simulations (PDF)

AUTHOR INFORMATION

Corresponding Author

Sandilya V. B. Garimella – Biological Sciences Division, Pacific Northwest National Laboratory, Richland, Washington 99354, United States; orcid.org/0000-0001-6649-9842; Email: sandilya.garimella@pnnl.gov

Authors

Jung Y. Lee – Biological Sciences Division, Pacific Northwest National Laboratory, Richland, Washington 99354, United States

Ailin Li – Biological Sciences Division, Pacific Northwest National Laboratory, Richland, Washington 99354, United States

Venkatesh Kumar Prabhakaran – Physical Sciences Division, Pacific Northwest National Laboratory, Richland, Washington 99354, United States; orcid.org/0000-0001-6692-6488

Xin Zhang – Physical Sciences Division, Pacific Northwest National Laboratory, Richland, Washington 99354, United States; orcid.org/0000-0003-2000-858X

Christopher P. P. Harrilal – Biological Sciences Division, Pacific Northwest National Laboratory, Richland, Washington 99354, United States; orcid.org/0000-0003-0576-1709

Libor Kovarik – Physical Sciences Division, Pacific Northwest National Laboratory, Richland, Washington 99354, United States

Yehia M. Ibrahim – Biological Sciences Division, Pacific Northwest National Laboratory, Richland, Washington 99354, United States; orcid.org/0000-0001-6085-193X

Richard D. Smith – Biological Sciences Division, Pacific Northwest National Laboratory, Richland, Washington 99354, United States; orcid.org/0000-0002-2381-2349

Author Contributions

§

J.Y.L. and A.L. contributed equally to this work.

Notes

The authors declare no competing financial interest.

ACKNOWLEDGMENTS

This work was performed with support from the Open Call Initiative of the Laboratory-Directed Research and Development Program at PNNL. This work was partially supported by and utilized the capabilities developed under the support of the NIH National Institute of General Medical Sciences (P41 GM103493-10, R01 GM130709-01, and R01 CA283818-01). This project was performed in the Environmental Molecular Sciences Laboratory, a DOE OBER national scientific user

facility on the PNNL campus. PNNL is a multiprogram national laboratory operated by Battelle for the DOE under contract DE-AC05-76RL01830. Authors gratefully acknowledge discussions with Dr. Amar Parvate regarding the TEM data and understanding of the same.

REFERENCES

- (1) Ray, S.; Tillo, D.; Boer, R. E.; Assad, N.; Barshai, M.; Wu, G.; Orenstein, Y.; Yang, D.; Schneekloth, J. S.; Vinson, C. *ACS Chem. Biol.* **2020**, *15* (4), 925–935.
- (2) Anisimov, S. V.; Khavinson, V. K.; Anisimov, V. N. *Neuroendocrinol. Lett.* **2004**, *25* (1–2), 87–93.
- (3) Lin, S.; Wang, D.; Zhang, L.; Jin, Y.; Li, Z.; Bonaccorso, E.; You, Z.; Deng, X.; Chen, L. *Advanced Science* **2021**, *8* (16), 2101331.
- (4) Castrovilli, M. C.; Tempesta, E.; Cartoni, A.; Plescia, P.; Bolognesi, P.; Chiarinelli, J.; Calandra, P.; Cicco, N.; Verraastro, M. F.; Centonze, D.; et al. *ACS Sustainable Chem. Eng.* **2022**, *10* (5), 1888–1898.
- (5) Bean, G. J.; Jaeger, P. A.; Bahr, S.; Ideker, T. *PLoS One* **2014**, *9* (1), No. e85177.
- (6) Li, X.; Liu, B.; Pei, B.; Chen, J.; Zhou, D.; Peng, J.; Zhang, X.; Jia, W.; Xu, T. *Chem. Rev.* **2020**, *120* (19), 10793–10833.
- (7) Franchetti, V.; Solka, B. H.; Baitinger, W. E.; Amy, J. W.; Cooks, R. G. *Int. J. Mass Spectrom.* **1977**, *23* (1), 29–35.
- (8) Tata, A.; Salvitti, C.; Pepi, F. *Int. J. Mass Spectrom.* **2020**, *450*, 116309.
- (9) Laskin, J.; Johnson, G. E.; Warneke, J.; Prabhakaran, V. *Angew. Chem., Int. Ed.* **2018**, *57* (50), 16270–16284.
- (10) Ghosh, J.; Cooks, R. G. *TrAC, Trends Anal. Chem.* **2023**, *161*, 117010.
- (11) Prabhakaran, V.; Mehdi, B. L.; Ditto, J. J.; Engelhard, M. H.; Wang, B.; Gunaratne, K. D. D.; Johnson, D. C.; Browning, N. D.; Johnson, G. E.; Laskin, J. *Nat. Commun.* **2016**, *7* (1), 11399.
- (12) Ran, W.; Walz, A.; Stoiber, K.; Knecht, P.; Xu, H.; Papageorgiou, A. C.; Huettig, A.; Cortizo-Lacalle, D.; Mora-Fuentes, J. P.; Mateo-Alonso, A.; et al. *Angew. Chem.* **2022**, *134* (14), No. e202111816.
- (13) Esser, T. K.; Böhning, J.; Fremdling, P.; Agasid, M. T.; Costin, A.; Fort, K.; Konijnenberg, A.; Gilbert, J. D.; Bahm, A.; Makarov, A.; et al. *PNAS Nexus* **2022**, *1* (4), pgac153.
- (14) Laskin, J. *Int. J. Mass Spectrom.* **2015**, *377*, 188–200.
- (15) Prabhakaran, V.; Johnson, G. E.; Laskin, J. *Curr. Opin. Electrochem.* **2023**, *40*, 101310.
- (16) Mikhailov, V. A.; Mize, T. H.; Benesch, J. L.; Robinson, C. V. *Anal. Chem.* **2014**, *86* (16), 8321–8328.
- (17) Verbeck, G.; Hoffmann, W.; Walton, B. *Analyst* **2012**, *137* (19), 4393–4407.
- (18) Fan, K.; Cao, C.; Pan, Y.; Lu, D.; Yang, D.; Feng, J.; Song, L.; Liang, M.; Yan, X. *Nat. Nanotechnol.* **2012**, *7* (7), 459–464.
- (19) Uchida, M.; Kang, S.; Reichhardt, C.; Harlen, K.; Douglas, T. *Biochim. Biophys. Acta, Gen. Subj.* **2010**, *1800* (8), 834–845.
- (20) Wang, C.; Liu, Q.; Huang, X.; Zhuang, J. *J. Mater. Chem. B* **2023**, *11*, 4153–4170.
- (21) Ochner, H.; Rauschenbach, S.; Malavolti, L. *Essays Biochem.* **2023**, *67* (2), 151–163.
- (22) Wu, X.; Delbianco, M.; Anggara, K.; Michnowicz, T.; Pardo-Vargas, A.; Bharate, P.; Sen, S.; Pristl, M.; Rauschenbach, S.; Schlickum, U.; et al. *Nature* **2020**, *582* (7812), 375–378.
- (23) Rinke, G.; Rauschenbach, S.; Schrettl, S.; Hoheisel, T. N.; Blohm, J.; Gutzler, R.; Rosei, F.; Frauenrath, H.; Kern, K. *Int. J. Mass Spectrom.* **2015**, *377*, 228–234.
- (24) Kottke, P. A.; Lee, J. Y.; Jonke, A. P.; Seneviratne, C. A.; Hecht, E. S.; Muddiman, D. C.; Torres, M. P.; Fedorov, A. G. *Anal. Chem.* **2017**, *89* (17), 8981–8987.
- (25) Sun, M.; Sun, J.; Yang, Y.; Wang, Y.; Lu, H.; Ouyang, J.; Na, N. *Talanta* **2019**, *197*, 36–41.

- (26) Johnson, G. E.; Prabhakaran, V.; Browning, N. D.; Mehdi, B. L.; Laskin, J.; Kottke, P. A.; Fedorov, A. G. *Batteries Supercaps* **2018**, *1* (3), 97–101.
- (27) Prabhakaran, V.; Romo, J.; Bhattarai, A.; George, K.; Norberg, Z. M.; Kalb, D.; Aprà, E.; Kottke, P. A.; Fedorov, A. G.; El-Khoury, P. Z.; et al. *Chem. Commun.* **2022**, *58* (65), 9060–9063.
- (28) Badu-Tawiah, A. K.; Wu, C.; Cooks, R. G. *Anal. Chem.* **2011**, *83* (7), 2648–2654.
- (29) Espy, R. D.; Badu-Tawiah, A.; Cooks, R. G. *Curr. Opin. Chem. Biol.* **2011**, *15* (5), 741–747.
- (30) Walton, B. L.; Verbeck, G. F. *Anal. Chem.* **2014**, *86* (16), 8114–8120.
- (31) Walton, B. L.; Hoffmann, W. D.; Verbeck, G. F. *Int. J. Mass Spectrom.* **2014**, *370*, 66–74.
- (32) Hoffmann, W.; Verbeck, G. *Appl. Spectrosc.* **2013**, *67* (6), 656–660.
- (33) Gillig, K. J.; Chen, C.-H. *Mass Spectrom.* **2014**, *3* (Special_Issue), S0032.
- (34) Rose, B. S.; May, J. C.; Reardon, A. R.; McLean, J. A. *J. Am. Soc. Mass Spectrom.* **2022**, *33* (7), 1229–1237.
- (35) Hollerbach, A. L.; Li, A.; Prabhakaran, A.; Nagy, G.; Harrilal, C. P.; Conant, C. R.; Norheim, R. V.; Schimelfenig, C. E.; Anderson, G. A.; Garimella, S. V.; et al. *Anal. Chem.* **2020**, *92* (11), 7972–7979.
- (36) Deng, L.; Webb, I. K.; Garimella, S. V.; Hamid, A. M.; Zheng, X.; Norheim, R. V.; Prost, S. A.; Anderson, G. A.; Sandoval, J. A.; Baker, E. S.; et al. *Anal. Chem.* **2017**, *89* (8), 4628–4634.
- (37) Li, A. L.; Nagy, G.; Conant, C. R.; Norheim, R. V.; Lee, J. Y.; Giberson, C.; Hollerbach, A. L.; Prabhakaran, V.; Attah, I. K.; Chouinard, C. D.; et al. *Anal. Chem.* **2020**, *92* (22), 14930–14938.
- (38) Deng, L. L.; Ibrahim, Y. M.; Hamid, A. M.; Garimella, S. V. B.; Webb, I. K.; Zheng, X. Y.; Prost, S. A.; Sandoval, J. A.; Norheim, R. V.; Anderson, G. A.; et al. *Anal. Chem.* **2016**, *88* (18), 8957–8964.
- (39) Garimella, S. V.; Ibrahim, Y. M.; Webb, I. K.; Ipsen, A. B.; Chen, T.-C.; Tolmachev, A. V.; Baker, E. S.; Anderson, G. A.; Smith, R. D. *Analyst* **2015**, *140* (20), 6845–6852.
- (40) Garimella, S. V.; Nagy, G.; Ibrahim, Y. M.; Smith, R. D. *TrAC, Trends Anal. Chem.* **2019**, *116*, 300–307.
- (41) Appelhans, A. D.; Dahl, D. A. *Int. J. Mass Spectrom.* **2005**, *244* (1), 1–14.
- (42) Dahl, D. A.; McJunkin, T. R.; Scott, J. R. *Int. J. Mass Spectrom.* **2007**, *266* (1–3), 156–165.
- (43) Lai, H.; McJunkin, T. R.; Miller, C. J.; Scott, J. R.; Almirall, J. R. *Int. J. Mass Spectrom.* **2008**, *276* (1), 1–8.
- (44) López, X.; Carbó, J. J.; Bo, C.; Poblet, J. M. *Chem. Soc. Rev.* **2012**, *41* (22), 7537–7571.
- (45) WS, R. *ImageJ*; US National Institutes of Health, Bethesda, Maryland, USA, 2011 <http://imagej.nih.gov/ij/>.
- (46) Warneke, J.; McBriarty, M. E.; Riechers, S. L.; China, S.; Engelhard, M. H.; Aprà, E.; Young, R. P.; Washton, N. M.; Jenne, C.; Johnson, G. E.; et al. *Nat. Commun.* **2018**, *9* (1), 1889.
- (47) Wojcik, R.; Nagy, G.; Attah, I. K.; Webb, I. K.; Garimella, S. V.; Weitz, K. K.; Hollerbach, A.; Monroe, M. E.; Ligare, M. R.; Nielson, F. F.; et al. *Anal. Chem.* **2019**, *91* (18), 11952–11962.
- (48) Jacobs, D. J. *Phys.: Condens. Matter* **1995**, *7* (6), 1023–1045.
- (49) Alvarez, J.; Futrell, J. H.; Laskin, J. *J. Phys. Chem. A* **2006**, *110* (4), 1678–1687.
- (50) Shen, J.; Yim, Y. H.; Feng, B.; Grill, V.; Evans, C.; Cooks, R. G. *Int. J. Mass Spectrom.* **1999**, *182–183*, 423–435.
- (51) Benner, W. H.; Lewis, G. S.; Hering, S. V.; Selgelke, B.; Corzett, M.; Evans, J. E.; Lightstone, F. C. *Anal. Chem.* **2012**, *84* (5), 2498–2504.
- (52) Huntley, A. P.; Hollerbach, A. L.; Prabhakaran, A.; Garimella, S. V.; Giberson, C. M.; Norheim, R. V.; Smith, R. D.; Ibrahim, Y. M. *Anal. Chem.* **2023**, *95* (9), 4446–4453.